Scientific Reports

https://doi.org/10.1038/s41598-026-42250-3

Article in Press

Experimental crystallization of analcime zeolite from clay and feldspar precursors

Received: 22 June 2025

Accepted: 25 February 2026

Published online: 05 March 2026

Cite this article as: Bello A.M., Salisu A.M., Amao A.O. *et al.* Experimental crystallization of analcime zeolite from clay and feldspar precursors. *Sci Rep* (2026). https://doi.org/10.1038/s41598-026-42250-3

Abdulwahab Muhammad Bello, Anas Muhammad Salisu, Abduljamiu O. Amao, Olalekan S. Alade, Mohamed Mahmoud & Khalid Al-Ramadan

Experimental Crystallization of Analcime Zeolite from Clay and Feldspar Precursors

Abdulwahab Muhammad Bello[1], Anas Muhammad Salisu[1], Abduljamiu O. Amao[1], Olalekan S. Alade[1], Mohamed Mahmoud[3], and Khalid Al-Ramadan[1,2*]

[1]Centre for Integrative Petroleum Research, College of Petroleum Engineering & Geosciences, King Fahd University of Petroleum & Minerals, Dhahran, Saudi Arabia

[2]Geosciences Department, College of Petroleum Engineering & Geosciences, King Fahd University of Petroleum & Minerals, Dhahran, Saudi Arabia.

[3]Department of Petroleum Engineering, College of Petroleum Engineering & Geosciences, King Fahd University of Petroleum & Minerals, Dhahran, Saudi Arabia.

*Corresponding Author: ramadank@kfupm.edu.sa

Abstract

Analcime is a common authigenic mineral in siliciclastic rocks and has widespread industrial applications in catalysis and ceramic production. Although its formation from volcanic glass has been extensively studied, the role of clay minerals and feldspar precursors in its genesis remains poorly constrained. This study investigates the hydrothermal formation of

analcime and associated zeolites from arkosic sandstone of the Oligocene-Miocene Al Wajh Formation, NW Saudi Arabia using Na_2CO_3 solutions (0.1 M and 0.5 M) at 80, 150, 200, and 250 ○C for 336 hours. The results indicate that analcime crystallized through the dissolution of feldspars, kaolinite, smectite, and illite, forming cubic to trapezohedral crystals. Mordenite and chabazite formed as minor zeolite phases at ≥200 ○C, associated with higher silica activity and the breakdown of silica gel, smectite, and illite. Analcime precipitated as grain-coating, replacive, and pore-filling cement, with intercrystalline pores reaching up to 9.7 µm in size. The synthesised analcime may enhance the mechanical stability of the sandstone framework by reducing susceptibility to compaction. Furthermore, if exposed to acidic meteoric waters, dissolution of analcime could generate secondary intracrystalline porosity that could significantly improve the overall reservoir quality of the sandstone.

Key words: analcime; zeolites; diagenesis, clay minerals; feldspars; reservoir quality

1. Introduction

Over the last few decades, zeolites have attracted increasing global attention due to their broad economic and scientific significance [1–7]. They are widely used in numerous industrial applications, including pollution control, soil conditioners and fertilizers, gas purification, petroleum production etc. [8,9]. Therefore, zeolites are often regarded as the “mineral future” in many countries, where significant efforts are underway to explore, develop, and utilize these resources effectively [10,11]. Zeolites are

naturally-occurring, hydrated aluminosilicate minerals that occur in a variety of igneous, low-grade metamorphic and sedimentary rocks, with over 20 known mineral species [4,12]. However, the most widely known species of zeolites are analcime, clinoptilolite, chabazite, erionite, mordenite, and phillipsite [8]. Analcime occurs in clastic sedimentary rocks spanning a wide range of geological ages, lithologies, and depositional environments in basins worldwide [3,6]. For instance, analcime has been documented in the Mesozoic Stuttgart Formation of northern Germany [7]; the Eocene Shahejie Formation in the Bohai Basin of northeastern China [13]; the Eocene Green River Formation of Utah, USA [14]; and the Pleistocene strata of the Lake Lewis Basin in central Australia [15] etc. In addition, analcime can form during steam injection for heavy oil recovery and as a result of hot fluid circulation in geothermal systems [16]. Although basins reporting analcime occurrences are not particularly extensive in number or scale, its presence within reservoir rocks can significantly influence reservoir quality by modifying porosity and permeability [17,18].

Diagenesis is widely recognized as the primary mechanism responsible for the formation of authigenic minerals in siliciclastic rocks [19–33,33–39,39,40,40,41,41,42,42,43,43–49]. Analcime is commonly reported to form through the diagenetic transformation of clinoptilolite, which in turn forms from hydration of abundant volcanic glass during shallow burial diagenesis. Iijima[2] noted that this transformation occurs at temperatures ranging between 84 and 91 °C. Numerous studies have therefore focused on investigating the origin of analcime through the transformation of clinoptilolite [1,2,50–52].

In addition, clay minerals and feldspars are frequently cited as potential precursors for authigenic analcime [6,53]. However, the mechanisms governing analcime formation from clay and feldspar precursors remain poorly constrained. This knowledge gap is chiefly because the reaction frequently occurs at depths > 1000 m [6], where precursor phases are commonly consumed during diagenesis and thus become difficult to identify in the rock record.

To address this limitation, the present study employs controlled hydrothermal-reactor experiments to investigate the crystallization of analcime from clay and feldspar precursors using an arkosic braided-river sandstone from the Oligocene-Miocene Al Wajh Formation (NW Saudi Arabia; Fig. 1A-C). The sedimentology and early diagenetic features of the Al Wajh Formation have been described in detail by Bello[54]. The specific objectives of the present study are to:

1) Characterize the mode of occurrence and textural evolution of diagenetic analcime derived from clay and feldspar precursors.
2) Investigate the formation of associated zeolite phases during the hydrothermal experiments.
3) Evaluate the influence of Na concentration on the formation and thermal stability of the synthesized analcime.

2. Geological background of the Al Wajh sample

The present study utilized an outcrop, sandstone sample from the Al Wajh Formation, situated in the Midyan Basin, northwest Saudi Arabia (Fig. 1A-C). The sampled unit has been interpreted as a braided fluvial sandstone

[54]. The Al Wajh Formation represents the oldest syn-rift succession in the Midyan Basin, deposited during the Early Oligocene to Early Miocene (Fig. 1C)The sedimentology, depositional facies, diagenesis, and reservoir characteristics have been extensively documented in previous studies [54–57]. Overall, the Al Wajh Formation is interpreted to have been deposited in predominantly alluvial, fluvial, and lacustrine settings, locally influenced by marginal marine conditions [56,58].

The Al Wajh Formation was selected for this study because of its arkosic composition, the presence of clay minerals, and its abundance of plutonic and volcanic fragments [54]. Additionally, the formation provides an excellent natural laboratory for investigating early diagenetic processes and their impact on reservoir quality, as it has undergone only shallow burial diagenesis [54].

3. Materials and methods

3.1 Analytical procedures

Bulk and clay-fraction X-ray diffraction (XRD) analyses were conducted on both pre- and post-reacted samples of the studied Al Wajh sandstone primarily to achieve qualitative identification of mineral phases and to document and mineralogical changes induced during the experiments, following the established criteria for sandstone and clay mineral analysis outlined by Bello[59,60] and Salisu[61,62]. Due to the inherent limitations of XRD for precise mineral quantification, particularly in heterogeneous sandstones and clay-rich fractions, the analyses were intentionally focused on mineral peak identification rather than absolute quantification.

Bulk samples were gently crushed to a fine powder (<63 μm) and analyzed as random mounts, whereas the clay fraction (<2 μm) was separated by sedimentation after dispersion in deionized water, following the procedure described by [60,63]. XRD measurements were performed using a Malvern Empyrean PANanalytical diffractometer operated at 45 kV and 40 mA. Random powder mounts were scanned over a 2θ range of 4–70° using CuKα radiation, with a step size corresponding to a counting time of 8.7 s per step. Oriented clay mounts were prepared and analyzed under air-dried conditions to enhance basal reflections and facilitate clay mineral identification.

Mineral phase identification was performed using HighScore Plus software (v. 4.9) equipped with the ICDD PDF-4+ (2024) mineralogical database. Quantitative phase analysis of bulk samples was carried out using the Rietveld refinement method implemented in HighScore Plus. The refinement procedure included background modeling, refinement of scale factors, zero shift, unit cell parameters, and peak profile parameters. Phase weight percentages were calculated from the refined scale factors using the crystallographic models incorporated in the database.

Refinement quality was evaluated using standard agreement indices (e.g., Rwp, Rp, and goodness-of-fit), and refinements were accepted once convergence was achieved without systematic misfit in the difference plots. Although Rietveld refinement provides quantitative phase estimates with high numerical precision, the practical analytical uncertainty of quantitative XRD analysis in heterogeneous sandstone samples is typically

on the order of ±1–3 wt.% for major phases and higher for minor phases, owing to factors such as sample preparation, grain statistics, preferred orientation, and microstructural effects. Thus, the mineral abundances are interpreted within this expected uncertainty, and small differences between samples are discussed in terms of overall trends rather than precise numerical variations.Clay mineral abundances were assessed qualitatively to semi-quantitatively based on relative basal peak intensities from oriented mounts, following established XRD clay mineral analysis protocols [63]. Owing to the effects of preferred orientation, variable crystallinity, mixed-layering, and interlayer hydration, clay mineral proportions are expressed as relative abundances, and no attempt was made to derive fully quantitative clay mineral contents. XRD interpretations were integrated with petrographic observations and SEM–EDX analyses to strengthen mineral identification and mitigate uncertainties inherent in clay mineral XRD analysis.

Standard petrographic thin section for the pre-reacted Al Wajh sandstone was prepared and studied using an Olympus BX53F petrographic microscope to investigate the primary, framework composition, pore-filling matrix, and secondary diagenetic cements. In addition, the petrographic analysis was chiefly conducted to complement the XRD data and to establish the average sandstone composition. Compositional point counting (using 300 points) was conducted on the pre-reacted sample using a Petrog software package. Additionally, the software was employed to establish the textural characteristics of the pre-reacted sample (e.g.,

grain size and sorting), by measuring the longest axes of 100 detrital quartz and undegraded feldspar gains.

Stub-mounted samples of both the reacted and unreacted sandstones of the Al Wajh Formation were investigated using a Zeiss Gemini 550 scanning electron microscope (SEM), which was fitted with an Aztec energy dispersive X-ray spectrometer (EDX). The samples were coated with 30 nm palladium-gold using Quorum QR150R sputter coater prior to running the SEM analysis and were analyzed at the voltage and current ranging between 2 and 20 kV and 100 and 2 nA, respectively.

3.2 Hydrothermal-reactor experiments

Hydrothermal-reactor experiments were conducted using a mechanically stirred autoclave at the Experimental Diagenesis Laboratory, Center for Integrative Petroleum Research, College of Petroleum Engineering and Petroleum Geoscience, King Fahd University of Petroleum and Minerals, Saudi Arabia. The starting material, Al Wajh sandstone, was divided into eight equal portions (approximately 20 g each). The samples were reacted with 0.1 M and 0.5 M Na_2CO_3 solutions at constant temperatures of 80, 150, 200, 250 $^{\circ}$C for 336 hours each (Table 1), following the experimental setup and procedures described by Bello[60,64].

Experiments were carried out in 500 mL reactor vessels containing 200 mL of solution, corresponding to a fluid–rock ratio of 10:1. The initial pressure was approximately 44 bar at room temperature; pressure increased progressively with temperature, and the final pressures attained during each experiment are reported in Table 1. All experiments were

conducted under strictly closed-system conditions. Upon completion, the reactors were allowed to cool to room temperature (25 °C), after which final pH measurements were recorded (Table 1). Initial and final pH values of the solutions are provided in Table 1.

4. Results

4.1 Pre-reacted sandstone composition

The Al Wajh sample utilized in the study is a medium-grained and well sorted sandstone, with a mean grain size of 0.43 mm. Petrographic point-count analysis indicates that the framework is dominated by detrital monocrystalline quartz (40.5 vol%), microcline (4 vol%), orthoclase (10.1 vol%), and plagioclase (5 vol%). Mica is present as minor biotite (1 vol%) and muscovite (1 vol%). Lithic fragments occur as felsic plutonic (1 vol%) and siltstone (1 vol%) rock fragments.

The pore-filling clay matrix occurs in trace amounts (0.5 vol%), whereas grain-coating clay reaches up to 7 vol%; both are predominantly smectitic in composition based on SEM–EDX analysis. Kaolinite is present mainly as a grain-replacive cement (3.5 vol% of total rock volume), replacing detrital feldspar and felsic plutonic rock fragments.

According to the classification scheme of Folk (1980), the pre-reacted sandstone is compositionally classified as arkosic, with an average framework composition of Q65F32R3 (where Q = quartz; F = feldspar; and R = rock fragments).

Bulk XRD analysis of the pre-reacted Al Wajh sandstone indicates that the dominant framework minerals are quartz (67 wt%), orthoclase (11 wt%), microcline (9 wt%), and albite (11 wt%). Accessory phases include muscovite (1 wt%), chlorite (1 wt%), kaolinite (1 wt%), and dickite (trace amounts).

4.2 Post-reacted sandstone composition

The mineralogical composition of the post-reacted Al Wajh sandstone was established using both bulk and clay-fraction XRD analyses (Fig. 2A-D). Bulk XRD results indicate that the framework minerals of the treated samples are dominated by quartz, albite, and orthoclase (Fig. 2A-D). Clay minerals consist mainly of mixed-layer illite-smectite, kaolinite, illite, and chlorite (Fig. 2C & D).

During experiments conducted at 150, 200, and 250 ○C, mixed-layer illite-smectite, chlorite, and kaolinite were progressively consumed, as evidenced by the reduction or disappearance of characteristic kaolinite and chlorite reflections in the clay-fraction diffractograms (Fig. 2C, D).

Analcime represents the principal authigenic zeolite phase formed at temperatures between 150 and 250 °C (Fig. 2A–D).

4.3 Crystal shape and size of analcime

Four distinct crystal morphologies were observed in the synthesized analcime: (1) spherical (Fig. 3A); (2) cubic (Fig. 3B); (3) trapezohedral (Fig. 3C & D); and (4) interpenetration twins (aggregates; Fig. 3E & F) crystals. The spherical analcime crystals (Fig. 3A) occur mainly as grain coatings

and range in diameters from 9.6 to 14.7 µm (average 11.1). These crystals are most well developed at 200 ○C. In contrast, cubic analcime crystals are smaller, with diameters ranging from 3.4 to 5.6 µm (average 4.4 µm). The trapezohedral crystals are typically euhedral and occur as discrete individuals (Fig. 3C & D). The diameters across the trapezohedral crystal tops range from 3.1 to 5.5 µm (average 4.3), while individual crystal faces measure between 1.2 to 3.9 µm (average 2.3 µm). This morphology was observed only in experiments conducted at 200 °C.. Aggregate analcime crystals commonly consist of intergrown cubic and polygonal forms, often displaying interpenetration twinning (Fig. 3E, F). The cubic aggregates range from 1.6 to 4.5 µm in diameter (average 2.8 µm), whereas individual cubic crystals within these aggregates measure 0.4 to 1.0 µm (average 0.7 µm). Polygonal crystal aggregates (Fig. 3F) are larger, with diameters ranging from 21.6 to 23.9 µm (average 22.9 µm).

4.4 Mode of occurrence of analcime

The studied analcime crystals occur in 4 main types: 1) grain-replacive; 2) clay-replacive; 3) grain-coating; and 4) pore-filling cements.

4.4.1 Grain-replacive analcime

Crystals of analcime often occur as diagenetic replacements of detrital grains, including K-feldspar and albite (Fig. 4A & B). The replacement commonly occurs along the edges of partly to pervasively dissolved feldspar grains (Fig. 4C) or within their interior parts (Fig. 4A). SEM analysis has shown that both the replacement of albite and K-feldspar

grains by analcime seems to occur in a dissolution-precipitation fashion (Fig. 4A-E). However, SEM observations reveal that the dissolution of albite resulted in the formation of amorphous aluminosilica gel, around and upon which analcime precipitated (Fig. 4E). Other minor zeolites formed include mordenite and chabazite (Fig. 4F). Occasionally, a rod-like and fibrous mordenite nucleated on a silica gel (Fig. 4F). Additionally, the spherical silica gel develops on severely etched feldspar grain (Fig. 4G), and, in some other instances, authigenic smectite (montmorillonite) grows perpendicular to the etched feldspar surface (Fig. 4H).

4.4.2 Clay-replacive analcime

Diagenetic analcime replaces kaolinite, illite, and smectite-rich clays (Fig. 5A-F). For instance, cubic, spherical, and cubic aggregate of analcime crystals developed in the vicinity of smectitic and illitic clays (Fig. 5A). Additionally, authigenic analcime commonly engulfs the clay they replace (e.g., kaolinite and smectite; Fig. 5B & C). Furthermore, SEM observations indicate that, at higher temperature, smooth, aggregate analcime crystals significantly consume kaolinite (Fig. 5B), smectite (Fig. 5C), and illite (Fig. 5D, E & F), with the illite crystals almost completely consumed during the replacement (Fig. 5E & F).

4.4.3 Grain-coating and pore-filling analcime

Spherical crystals of analcime grow on and around detrital quartz and feldspars (e.g., Fig. 3A). The crystals range in diameter from 9.6 to 14.7 μm, averaging 11.1. They provide partial to complete cover around the

detrital grains. Occasionally, the spherical grain-coating crystals aggregate grow into the intergranular pore, thereby developing into a pore-filling cement (Fig. 3A). SEM observations reveal that the grain-coating analcime crystals replace smectitic, grain-coating clays (Fig. 3A). Analcime occurs as a pore-filling cement. Pore-filling analcime consists of spherical, trapezohedral, and interpenetration crystals, filling and reducing primary intergranular porosity. Blocky, pore-filling aggregates of analcime crystals over 10 μm and often block pore throats. It has been observed that the pore-filling analcime crystals are more developed at high temperatures 200 and 250 °C.

4.5 Other minor zeolites synthesized

SEM-EDX analysis revealed the development of two additional, minor zeolites phases (mordenite and chabazite), particularly in experiments conducted at elevated temperatures between 200 and 250 °C (Fig. 6A-F; Table 2). Mordenite appears as acicular, needle-like crystals around smectitic clays and detrital feldspars (Fig. 6A & B), while chabazite forms euhedral, pseudohexagonal platelets arranged in distinctive stacked rosette-like aggregates in smectite vicinity (Fig. 6C & D). Individual mordenite fibres range in length from 10.7 to 44.8 μm (av. 23.3 μm) and in width from 0.3 to 0.6 μm wide (av. 0.4 μm). Both mordenite and chabazite developed in close association with detrital feldspar and clay minerals, often forming as replacive phases or and pore-filling cements. Chabazite platelets range in diameter from 7.8 to 36.4 μm (av. 18.9 μm), while the entire rosettes structures vary in thickness from 7.2 to 47.3 μm

(av. 27.8 µm). The rosette morphology of chabazite coupled with its elemental composition are typical of those described by Welton[16]. Additionally, the chabazite is characterized by abundant intercrystalline porosity (Fig. 6C & D), with pore diameters ranging in size from 0.6 to 5.3 µm, averaging 2.6. While majority of the synthesized mordenite and chabazite occur as replacements of feldspar and clay minerals, mordenite and analcime grew on aluminosilica gels (Fig. 6E & F), formed from the dissolution of both feldspars and clay minerals

4.6 Chemical Composition of Analcime

4.6.4 Major oxides

The major oxide compositions of the synthesized zeolites were determined using SEM-EDX analysis (Table 2). The major oxide data show clear compositional contrasts among analcime, mordenite, and chabazite. SiO_2 is the dominant oxide in all samples. Analcime displays consistently high and relatively uniform SiO_2 contents (mean 63–67 wt.%). Mordenite shows broader variation, particularly in sample AWB3 (36–70 wt.%, 52 ± 12 wt.%). Chabazite contains lower SiO_2 (50 ± 5 wt.%).

Al_2O_3 contents in analcime range from approximately 19 to 23 wt.% and are similarly elevated in chabazite (18 ± 2 wt.%). Mordenite exhibits lower and more variable Al_2O_3, with means around 9–10 wt.% in AWB3 and AWB4 (Table 2). TiO_2 is negligible in nearly all samples.

FeO and MgO contents distinguish the mineral groups. Analcime contains low FeO (generally 1–3 wt.%) and negligible MgO. Mordenite shows higher

FeO (up to 8 ± 4 wt.%) and MgO (4–7 wt.%). Chabazite has intermediate FeO (6 ± 2 wt.%) and moderate MgO (5 ± 1 wt.%).

Marked differences are observed in Na_2O and CaO. Analcime is consistently Na-rich (10–14 wt.% Na_2O) and Ca-poor. Mordenite, especially AWB3, contains very high and variable Na_2O (25 ± 12 wt.%). Chabazite is characterized by high CaO (12 ± 6 wt.%) and comparatively low Na_2O (5 ± 1 wt.%). K_2O is generally low in analcime and slightly higher in mordenite and chabazite.

4.7 Porosity

Porosity within the synthesized analcime crystals is predominantly intercrystalline. This intercrystalline porosity is generally abundant and becomes more pronounced with increasing experimental temperature. In contrast, intracrystalline porosity, typically associated with crystal dissolution, is largely absent in the studied samples, as the analcime crystals underwent growth rather than dissolution under the experimental conditions. The intercrystalline porosity ranges in diameter from 0.2 to up to 9.7 μm, averaging 2.0. Aggregate cubic analcime crystals contain the least intercrystalline porosity, whereas the trapezohedral crystal shapes form the best intercrystalline porosity.

5. Discussion

5.1 Mechanisms of formation of zeolites

The formation of zeolites and feldspars in siliciclastic rocks, rather than clay minerals, is commonly attributed to elevated silica activity and high alkali-to-hydrogen ion (Na^+/H^+) ratios, and these conditions are typically favored by the presence of entrapped saline-alkaline water [1,6,12,61,65]. Our experimental findings support this interpretation, indicating that zeolite formation from arkosic sandstone cemented by kaolinite and smectitic clays is strongly influenced by both temperature and the alkalinity of the reacting solutions.

Several mechanisms have been proposed to account for the origin of authigenic zeolites in sandstones, including (1) alteration of precursor minerals such as zeolites or volcanic glass; (2) crystallization from amorphous aluminosilicate gels, which form during the dissolution of detrital silicates; (3) direct precipitation from slightly to moderately saline, alkaline pore fluids; and (4) water-rock interaction reactions involving detrital silicates (e.g., feldspars, kaolinite, smectite, or illite) and saline-alkaline pore water [6,66,67]. However, two primary mechanisms were responsible for the formation of zeolites observed in our study. The predominant pathway involved the dissolution of detrital feldspars and clay minerals (Figs. 5, 6, and 7), which released the essential elements such as Si and Al into the solution and subsequent precipitation of zeolites. While some of the Na^+ required for zeolite formation may have been derived from the dissolution of albite, the majority of the Na^+ was likely

supplied by the Na-rich experimental fluid. A secondary mechanism involved the crystallization of zeolites from intermediate aluminosilicate gels (Fig. 6E & F), which formed during early stages of precursor breakdown under elevated temperatures and alkaline conditions.

Our study indicates that the formation of analcime occurred primarily through a dissolution-precipitation mechanism, rather than by pseudomorphic replacement. This is attributed to the structural incompatibility between the framework analcime and that of its precursor minerals. Detrital feldspars, including both potassium feldspar and plagioclase (albite), exhibited varying degrees of dissolution under experimental conditions (Fig. 4A-E), thereby providing the essential Si, Al, and Na required for analcime formation. Analcime with different crystal morphologies subsequently precipitated in close proximity to these etched feldspar grains (Fig. 4A-E), indicating the spatial association between feldspar dissolution and zeolite nucleation. In addition, analcime crystals were observed to grow at the expense of partially to completely dissolved kaolinite, smectite, and illite (Fig. 5A-F), suggesting that clay minerals served as important precursors by supplying essential framework elements such as Si, Al, and Na. Evidence from SEM (Fig. 5B) and XRD analyses (Fig. 2C & D) have shown that kaolinite is almost completely consumed in the formation of analcime. This is particularly evident in the XRD patterns, where the primary kaolinite peak disappears entirely at experimental temperatures of 150, 200, and 250 $^{\circ}$C, which coincides with the formation of analcime at the same temperatures (Fig. 2C & D). Although the formation of analcime is strongly influenced by the

dissolution of both feldspar grains and clay minerals, the formation of minor zeolite phases (i.e., mordernite and chabazite) appears to be more closely linked to the dissolution of smectite and illite (Fig. 6A-D). The relatively high concentrations of Mg, K, and Ca detected in the mordernite and chabazite (Table 2) further corroborate this interpretation, suggesting that the breakdown of smectite and illite contributed these cations to the fluid, thereby promoting the formation of the minor zeolite phases under suitable conditions that the dissolution of these clays supply these essential elements for the formation of the minor zeolites. This highlights a compositional control in zeolite mineralogy, where the type and abundance of the precursor clays strongly influence the distribution and chemistry of the resulting zeolite minerals. Additionally, the occurrence of mordenite and chabazite exclusively at higher experimental temperatures (i.e., ≥200 $^{\circ}$C) suggests that their formation is favoured by high silica activity. However, the continued formation of feldspar-replacing smectite, despite the consumption of pre-existing smectite suggests slight to moderate alkaline formation that partly favours the formation of the smectite.

Although less common, a secondary pathway for the formation of analcime, mordenite, and chabazite in this study involved the intermediate development of amorphous aluminosilicate gels (Fig. 6E & F). These gels likely originated from the dissolution of silicate minerals, especially feldspars and clay phases (Fig. 4E & F). The gels subsequently underwent pervasive dissolution, which facilitated the nucleation of analcime, mordenite, and chabazite (Fig. 6E & F). This interpretation is consistent

with previous studies, which propose that zeolites can crystallize from aluminosilicate gels that initially precipitate from solution, indicating a two-step process involving gel formation followed by zeolite growth [8,43,68].

5.2 Condition of formation of analcime

The Si/Al ratio for zeolites is one of the key parameters that establish the conditions under which they formed [1,12]. Results of the measurements of Si/Al ratio for analcime in lacustrine samples from Bohai Bay Basin (China) and Jiuxi Basin (China) reveal that it ranges between 2.04 and 2.08, respectively, suggesting that the analcime probably formed under alkaline water conditions, with likely precursors consisting of detrital clays and other materials [6,69]. However, the Si/Al ratio for analcime from the lacustrine Junggar and Erlian Basins (China) show that it varies from 2.36 to 2.64, suggesting that they were formed in saline-alkaline pore water. In addition, while analcime with low Si/Al ratio are characterized by weak thermal stability, those with high Si/Al ratio commonly have moderate to high thermal stability [6]. In the present study, although preliminary Si/Al estimates were obtained from SEM–EDX analyses, these data are inherently semi-quantitative and do not provide sufficient precision for reliable structural formula calculations. Accordingly, definitive Si/Al ratios are not reported. Instead, the experimental conditions themselves provide strong constraints on the formation environment. All hydrothermal experiments were conducted under strongly alkaline conditions (initial pH ~10–11.5 at 25 °C) using 0.1 M and 0.5 M Na_2CO3 solutions (Table 1).

These alkaline conditions closely resemble those reported for natural lacustrine and saline–alkaline systems in which analcime commonly forms. Therefore, while precise compositional ratios cannot be robustly constrained in this study, the controlled alkaline chemistry of the experiments supports the interpretation that analcime crystallization was promoted by elevated pH and Na-rich fluids, comparable to natural alkaline diagenetic environments.

5.3 Implications for conventional and unconventional reservoirs

Zeolites can have significant impacts on the quality and petrophysical properties of clastic reservoirs [4,6,18]. As discussed, zeolites (e.g., analcime) preferentially form under highly alkaline conditions and, hence, are chemically unstable under acidic conditions [4,18]. During maturation of organic matter in hydrocarbon source rocks, carboxylic acids are generated and, as a result of pressure buildup and compaction, these acids (along with water) are expelled from the source rocks and migrate into arenitic sandstone beds up-dip [70,71]. This results in the dissolution of feldspar and analcime, thereby creating intragranular and intracrystalline porosities, respectively. For instance, Chen[17] reported that the analcime-cemented, Middle Permian Lower-Wuerhe Formation, Junggar Basin, (Northwest China) has 9 % porosity, more than 82 % of which is secondary porosity related to the dissolution of analcime. However, although our study did not investigate the dissolution of analcime, the synthesized analcime has the potential of secondary porosity generation, should exposure to acidic water occur.

Our study has also revealed that the formation of analcime consumes smectitic and illitic pore-filling matrix (Fig. 5A-E), thereby strengthening the framework grains and preventing the impact of mechanical compaction. In addition, the analcime crystals exhibit abundant, well-developed intercrystalline porosity that would potentially contribute to fluid storage and withdrawal. Therefore, the intercrystalline, micropores of analcime are highly significant in hydrocarbon reservoirs [4,10,72].

Lacustrine, deep to semi-deep fine-grained rocks (e.g., siltstone, mudstone, shale etc) are often well-cemented by analcime, mainly as pore-filling, fracture-filling, and grain-replacive cements [6,13]. Like other brittle minerals such as quartz, feldspar, and carbonate cement, analcime is characterized by high Young's Modulus and low Poisson's ratio, thereby favouring their fracturing and enhancing the unconventional reservoir characteristics of the host rocks [5,13].

5.4 Limitations of the study and future work

Our study has shown that the synthesized analcime crystals are morphologically comparable to those reported in ancient natural systems [6,7,18], suggesting that both experimental and naturally occurring analcime require appropriate precursor minerals and alkaline pore-fluid compositions for crystallization. However, the chemical characterization of the synthesized zeolites in this study was based on semi-quantitative SEM–EDX analyses, which do not provide the level of precision required for robust determination of mineral chemistry or key compositional parameters such as Si/Al ratios. Future studies should incorporate

wavelength-dispersive spectrometry (WDS) electron microprobe analyses to accurately establish the major-element chemistry of the synthesized zeolites and to reliably constrain important ratios, including Si/Al, that are critical for interpreting formation conditions and thermal stability.

In addition, thermodynamic stability modeling using geochemical software (e.g., Geochemist's Workbench, ACT2 module) would provide quantitative constraints on phase stability fields and reaction pathways under varying temperature, pH, and fluid compositions. Such modeling would strengthen the mechanistic interpretation of zeolite transformation sequences and allow better comparison between experimental results and natural diagenetic systems.

Furthermore, the experimental conditions cannot fully replicate natural diagenesis due to the relatively short duration of laboratory experiments compared to geological timescales. Although analcime in natural systems can form over a wide range of temperatures (including higher-temperature settings associated with igneous environments), the selected experimental temperatures may exceed those typical of sedimentary diagenetic systems. In addition, while the imposed alkaline conditions were sufficient to precipitate analcime, the simplified Na_2CO_3 solutions used in the experiments do not fully capture the chemical complexity of natural formation waters

Although recent studies have advanced our understanding of the origin, occurrence, and distribution of analcime in clastic sedimentary rocks, further work is needed to better constrain its dissolution mechanisms, the development of secondary intracrystalline porosity, and the effectiveness

of intercrystalline pore networks in facilitating fluid flow. In addition, geomechanical testing of analcime-cemented sandstones would help quantify its role in enhancing framework stability and resisting mechanical compaction. Additional experimental investigations are also required to determine the minimum pH threshold necessary for analcime formation, which would provide improved constraints on the alkalinity conditions required for its precipitation. Replicating similar hydrothermal experiments using modern, unconsolidated sand-dune or interdune sediments with variable feldspar and clay contents could further elucidate the early stages of alteration leading to analcime formation, particularly since the samples used in this study had already undergone shallow burial diagenesis prior to experimentation. The oxygen isotope composition of the synthesized analcime is vital for establishing their crystallization temperatures. However, if the isotope data appeared unreliable or challenging to measure, the oxygen isotopic analysis of other minerals commonly associated with analcime, such as chlorite or illite can be measured.

6. Conclusion

- The Tertiary, shallow-buried sandstone sample of the Al Wajh Formation (NW Saudi Arabia) was utilized for an autoclave experimental formation of various shapes of analcime crystals (including cubic, spherical, trapezohedral, and aggregates) at different experimental temperatures (80, 150, 200, 250 $^{\circ}$C) for 336 hours each (using a 0.1 and 0.5 M Na_2CO_3 synthetic solutions).

- The experimental results have provided evidence that that feldspar and clay minerals (e.g., kaolinite, smectite, and illite) were consumed to produce analcime and trace amounts of other zeolites (chabazite and mordenite).
- The synthesized analcime formed under strongly alkaline experimental conditions comparable to those reported for ancient, highly alkaline lacustrine environments. The synthesized analcime crystals were characterized by abundant, interconnected, and intercrystalline porosity (up to 9 μm in diameter). These crystals have the potentials to strengthen the sandstone's framework components, prevent mechanical compaction, reduce pore-filling clay matrix, and generate secondary intracrystalline porosity due to dissolution, thereby significantly improving the overall reservoir quality during deep burial.

References

(1) Hay, R. L. *Zoelites and Zeolites Reactions in Sedimentary*; Geological Society of America: New York, USA, 1966.

(2) Iijima, A. Effect of Pore Water to Clinoptilolite-Analcime-Albite Reaction Series. *Journal of the Faculty of Science, University of Tokyo, Section II* **1975**, *19*, 133–147.

(3) Iijima, A. Zeolites in Petroleum and Natural Gas Reservoirs in Japan: A Review. In *Natural Zeolites '93: Occurrence, Properties, Uses*; Int'l Comm Natural Zeolites: Brockport, New York, 1995; pp 99–114.

(4) Iijima, A. Zeolites in Petroleum and Natural Gas Reservoirs. *Reviews in Mineralogy and Geochemistry* **2001**, *45* (1), 347–402.

(5) Zhang, Y.; Shiyue, C.; Qing'ai, M.; Jihua, Y.; Xiugang, P.; Wenzhong, H. The Discovery of Analcite in Fine-Grained Sedimentary Rocks of the Second Member of Kongdian Formation in Cangdong Sag, Huanghua Depression: Implications for Early Digenetic Environment. *China Petroleum Exploration* **2015**, *20* (4), 37–43.

(6) Zhu, S.; Cui, H.; Jia, Y.; Zhu, X.; Tong, H.; Ma, L. Occurrence, Composition, and Origin of Analcime in Sedimentary Rocks of Non-Marine Petroliferous Basins in China. *Marine and Petroleum Geology* **2020**, *113*, 104164. https://doi.org/10.1016/j.marpetgeo.2019.104164.

(7) Niegel, S.; Franz, M. Depositional and Diagenetic Controls on Porosity Evolution in Sandstone Reservoirs of the Stuttgart Formation (North German Basin). *Marine and Petroleum Geology* **2023**, *151*, 106157. https://doi.org/10.1016/j.marpetgeo.2023.106157.

(8) Chipera, S. J.; Apps, J. A. Geochemical Stability of Natural Zeolites. *Reviews in Mineralogy and Geochemistry* **2001**, *45* (1), 117–161. https://doi.org/10.2138/rmg.2001.45.3.

(9) Auerbach, S. M.; Carrrado, K. A.; Dutta, P. K. *Handbook of Zeolite Science and Technology*; Marcel Dekker: New York, USA, 2003.

(10) Vernik, L. A New Type of Reservoir Rock in Volcaniclastic Sequences. *Bulletin* **1990**, *74*. https://doi.org/10.1306/0C9B23A3-1710-11D7-8645000102C1865D.

(11) Noh, J. H.; Boles, J. R. Origin of Zeolite Cements in the Miocene Sandstones, North Tejon Oil Fields, California. *SEPM JSR* **1993**, *Vol. 63*. https://doi.org/10.1306/D4267AD2-2B26-11D7-8648000102C1865D.

(12) Hay, R. L.; Sheppard, R. A. Occurrence of Zeolites in Sedimentary Rocks: An Overview. *Reviews in Mineralogy and Geochemistry* **2001**, *45* (1), 217–234. https://doi.org/10.2138/rmg.2001.45.6.

(13) Yao, G.; Li, L.; Cai, M.; Liu, Y. Mechanisms of Salinization in a Middle Eocene Lake in the Tanggu Area of the Huanghua Depression. *Marine and Petroleum Geology* **2017**, *86*, 155–167. https://doi.org/10.1016/j.marpetgeo.2017.05.028.

(14) Remy, R. R.; Ferrell, R. E. Distribution and Origin of Analcime in Marginal Lacustrine Mudstones of the Green River Formation, South-Central Uinta Basin, Utah. *Clays and Clay Minerals* **1985**, *37* (5), 419–432. https://doi.org/10.1346/CCMN.1989.0370505.

(15) English, P. M. Formation of Analcime and Moganite at Lake Lewis, Central Australia: Significance of Groundwater Evolution in Diagenesis. *Sedimentary Geology* **2001**, *143* (3–4), 219–244. https://doi.org/10.1016/S0037-0738(01)00063-X.

(16) Welton, J. E. *SEM Petrology Atlas*, Second.; AAPG: Tulsa, Oklahoma, USA, 2003.

(17) Chen, G. Zeolite minerals and their relation to oil and gas accumulation in the reservoir formations in Karamay Oil Field. *Acta Petrolei Sinica* **1992**, *13*, 44–51.

(18) Zhu, S.; Zhu, X.; Wang, X.; Liu, Z. Zeolite Diagenesis and Its Control on Petroleum Reservoir Quality of Permian in Northwestern Margin of Junggar Basin, China. *Sci. China Earth Sci.* **2012**, *55* (3), 386–396. https://doi.org/10.1007/s11430-011-4314-y.

(19) Worden, R. H.; Burley, S. D. Sandstone Diagenesis: The Evolution of Sand to Stone. In *Sandstone Diagenesis*; Worden, R. H., Burley, S. D., Eds.; International Association of Sedimentologists, 2003; pp 3–44. https://doi.org/10.1002/9781444304459.ch.

(20) Al-Ramadan, K. Diagenesis of Holocene Beachrocks: A Comparative Study between the Arabian Gulf and the Gulf of Aqaba, Saudi Arabia. *Arabian Journal of Geosciences* **2014**, *7* (11), 4933–4942. https://doi.org/10.1007/s12517-013-1127-7.

(21) Al-Ramadan, K. Illitization of Smectite in Sandstones: The Permian Unayzah Reservoir, Saudi Arabia. *Arabian Journal for Science and Engineering* **2014**, *39* (1), 407–412. https://doi.org/10.1007/s13369-013-0913-6.

(22) Al-Ramadan, K. Geochemical Signatures of Pervasive Meteoric Diagenesis of Early Miocene Syn-Rift Carbonate Platform, Red Sea, NW Saudi Arabia. *Geological Quarterly* **2017**, *61* (1), 239–250. https://doi.org/10.7306/gq.1334.

(23) Koeshidayatullah, A.; Al-Ramadan, K. Unraveling Cementation Environment and Patterns of Holocene Beachrocks in the Arabian Gulf and the Gulf of Aqaba: Stable Isotope Approach. *Geological Quarterly* **2014**, *58* (2), 207–216. https://doi.org/10.7306/gq.1144.

(24) Koeshidayatullah, A.; Chan, S. A.; Al-Ghamdi, M.; Akif, T.; Al-Ramadan, K. Discrimination of Inland and Coastal Dunes in Eastern Saudi Arabia Desert System: An Approach from Particle Size and Textural Parameter Variations. *Journal of African Earth Sciences* **2016**, *117*, 102–113. https://doi.org/10.1016/j.jafrearsci.2016.01.003.

(25) Al-Ramadan, K.; Franks, S. G.; Al-Shammari, S.; Rees, A.; Koeshidayatullah, A.; Abu-Khamsin, S. Depositional and Diagenetic Barriers, Baffles and Conduits: Permian – Carboniferous Unayzah Reservoir, Nuayyim Field, Central Saudi Arabia. *Journal of Petroleum Geology* **2017**, *40* (1), 85–103. https://doi.org/10.1111/jpg.12665.

(26) Herlambang, A.; Koeshidayatullah, A. I.; Amao, A. O.; Bello, A. M.; Al-Ghamdi, F.; Malik, M. H.; Al-Ramadan, K. A. H. Structural Diagenesis and Dolomitization of Cenozoic Post-Rift Carbonates in the Red Sea Rift Basin: A Multiproxy Approach. *Frontiers in Earth Science* **2022**, *10*. https://doi.org/10.3389/feart.2022.1037126.

(27) Alqubalee, A.; Salisu, A. M.; Bello, A. M.; Al-Hussaini, A.; Al-Ramadan, K. Characteristics, Distribution, and Origin of Ferruginous Deposits within the Late Ordovician Glaciogenic Setting of Arabia. *Scientific Reports* **2023**, *13* (1). https://doi.org/10.1038/s41598-023-45563-9.

(28) Bello, A. M.; Al-Ramadan, K.; Babalola, L. O.; Alqubalee, A.; Amao, A. O. Impact of Grain-Coating Illite in Preventing Quartz Cementation: Example from Permo-Carboniferous Sandstone, Central Saudi Arabia. *Marine and Petroleum Geology* **2023**, *149*, 1–14. https://doi.org/10.1016/j.marpetgeo.2022.106073.

(29) Bello, A. M.; Al-Ramadan, K.; Koeshidayatullah, A. I.; Amao, A. O.; Herlambang, A.; Al-Ghamdi, F.; Malik, M. H. Impact of Magmatic Intrusion on Diagenesis of Shallow Marine Sandstones: An Example from Qasim Formation, Northwest Saudi Arabia. *Front. Earth Sci.* **2023**, *11*, 1105547. https://doi.org/10.3389/feart.2023.1105547.

(30) Bello, A. M.; Usman, M. B.; Ismail, M. A.; Mukkafa, S.; Abubakar, U.; Kwami, I. A.; Al-Ramadan, K.; Amao, A. O.; Al-Hashem, M.; Salisu, A. M.; Kachalla, A.; Abubakar, M. B.; Maigari, A. S.; Chiroma, L. U. Linking Diagenesis and Reservoir Quality to Depositional Facies in Marginal to Shallow Marine Sequence: An Example from the Campano-Maastrichtian Gombe Sandstone, Northern Benue Trough, NE Nigeria. *Marine and Petroleum Geology* **2023**, 106386. https://doi.org/10.1016/j.marpetgeo.2023.106386.

(31) Bello, A. M.; Salisu, A. M.; Alqubalee, A.; Amao, A. O.; Al-Hashem, M.; Al-Hussaini, A.; Al-Ramadan, K. Diagenetic Controls on the Quality of Shallow Marine Sandstones: An Example from the Cambro-Ordovician Saq Formation, Central Saudi Arabia. *Journal of African Earth Sciences* **2024**, *215*, 105295. https://doi.org/10.1016/j.jafrearsci.2024.105295.

(32) Bello, A. M.; Al-Yaseri, A.; Amao, A. O.; Al-Ramadan, K. CO2 –Rock–Brine Interactions in Feldspar-Rich Sandstones That Underwent Intense Heating. *ACS Omega* **2024**, *9* (29), 31578–31585. https://doi.org/10.1021/acsomega.4c01256.

(33) Bello, A. M.; Usman, M. B.; Amao, A. O.; Al-Ramadan, K.; Al-Hashem, M.; Kachalla, A.; Abubakar, U.; Salisu, A. M.; Mukkafa, S.; Kwami, I.

A.; Aro, O. E.; Butt, M. N.; Maigari, A. S.; Yusuf, A.; Chiroma, L. U.; Akinsanpe, O. T. Diagenesis and Reservoir Quality Evolution of Estuarine Sandstones: Insights from the Cenomanian-Turonian Yolde Formation, Northern Benue Trough, NE Nigeria. *Marine and Petroleum Geology* **2024**, *169*, 1–24. https://doi.org/10.1016/j.marpetgeo.2024.107073.

(34) Bello, A. M.; Amao, A. O.; Koeshidayatullah, A. I.; Nazgah, M.; Alrowaie, M. A.; Herlambang, A.; Al-Ramadan, K. Petrological and Geochemical Characteristics of Ordovician Cherts in the Qasim Formation, NW Saudi Arabia: Understanding the Roles of Biogenic and Volcanic Activities. *Journal of Asian Earth Sciences* **2025**, 106483. https://doi.org/10.1016/j.jseaes.2024.106483.

(35) Salisu, A. M.; Alqubalee, A.; Bello, A. M.; Al-Hussaini, A.; Adebayo, A. R.; Amao, A. O.; Al-Ramadan, K. Impact of Kaolinite and Iron Oxide Cements on Resistivity and Quality of Low Resistivity Pay Sandstones. *Marine and Petroleum Geology* **2023**, *158*, 106568. https://doi.org/10.1016/j.marpetgeo.2023.106568.

(36) Salisu, A. M.; Algheryafi, H.; Bello, A. M.; Amao, A. O.; Al-Otaibi, B.; Al-Ramadan, K. Depositional and Diagenetic Controls on the Reservoir Quality of Marginal Marine Sandstones: An Example from the Early Devonian Subbat Member, Jauf Formation, Northwest Saudi Arabia. *Marine and Petroleum Geology* **2024**, *170*, 1–26. https://doi.org/10.1016/j.marpetgeo.2024.107147.

(37) Naveed Butt, M.; G. Franks, S.; Hussain, A.; Amao, A. O.; Muhammad Bello, A.; Al-Ramadan, K. Depositional and Diagenetic Controls on the

Reservoir Quality of Early Miocene Syn-Rift Deep-Marine Sandstones, NW Saudi Arabia. *Journal of Asian Earth Sciences* **2024**, *259*. https://doi.org/10.1016/j.jseaes.2023.105880.

(38) Butt, M. N.; Hussain, A.; Malik, M. H.; Amao, A. O.; Koeshidayatullah, A.; Olariu, C.; Bello, A. M.; Al-Ramadan, K. Depositional Architecture of Early Rift Non-Marine Systems and Implications for Reservoir Development: Oligocene to Miocene Al Wajh Formation, Midyan Basin of Red Sea, Saudi Arabia. *Marine and Petroleum Geology* **2024**, *168*, 107033. https://doi.org/10.1016/j.marpetgeo.2024.107033.

(39) Bello, A. M.; Al-Otaibi, B. D.; Salisu, A. M.; Algheryafi, H.; Amao, A. O.; Al-Ramadan, K. Petrography, Geochemistry, and Diagenetic Characteristics of the Early Silurian to Early Devonian Sequences, Northwest Saudi Arabia: Implications for Provenance, Tectonic Setting, Paleoclimate, and Paleoweathering. *Marine Geoscience and Energy Resources* **2026**, 207655. https://doi.org/10.1016/j.marger.2026.207655.

(40) Bello, A. M.; Amao, A. O.; Salisu, A. M.; Al-Ramadan, K. Clay-Driven Dolomitization at Moderate to High Temperatures: Evidence from Hydrothermal Experiments. *Geology* **2025**, *53* (12), 1040–1045. https://doi.org/10.1130/G53737.1.

(41) Abdulkarim, Y. A.; Bello, A. M.; Al-Ramadan, K. Provenance, Diagenesis and Reservoir Quality of the Aptian-Albian Bima Sandstone, Upper Benue Trough, NE Nigeria. *Journal of African Earth Sciences* **2026**, *234*, 105925. https://doi.org/10.1016/j.jafrearsci.2025.105925.

(42) Alfaraj, M. A.; Bello, A. M.; Salisu, A. M.; Al-Ramadan, K. Kaolinite Illitization Under Hydrothermal Conditions: Experimental Insight into Transformation Pathways. *Minerals* **2025**, *16* (1), 4. https://doi.org/10.3390/min16010004.

(43) Khoshnaw, A. S.; Alismail, D. N.; Bello, A. M.; Al-Ramadan, K. Experimental Investigation of Kaolinite–Zeolite Transformation: Insights from Al-Habala Area Saprolite, Abha, Saudi Arabia. *Minerals* **2025**, *15* (9), 920. https://doi.org/10.3390/min15090920.

(44) Saner, S.; Hassan, H. M.; Al-Ramadan, K. A.; Abdulghani, W. M. Mineralogical, Pore and Petrophysical Characteristics of the Devonian Jauf Sandstone Reservoir, Hawiyah Field, Eastern Saudi Arabia. *Journal of Petroleum Geology* **2006**, *29* (3), 257–272. https://doi.org/10.1111/j.1747-5457.2006.00257.x.

(45) Al-Ramadan, K. The Role of Diagenesis at Unconformities of the Paleozoic Siliciclastic Succession of Central Saudi Arabia: Implications for Reservoir Quality. *Arabian Journal of Geosciences* **2021**, *14*. https://doi.org/10.1007/s12517-021-06845-6.

(46) Eltom, H.; Abdullatif, O.; Makkawi, M.; Al-Ramadan, K.; Abdulraziq, A. Porosity Evolution within High-Resolution Sequence Stratigraphy and Diagenesis Framework: Outcrop Analog of the Upper Jurassic Arab-D Reservoir, Central Saudi Arabia. *Arabian Journal of Geosciences* **2015**, *8* (3), 1669–1690. https://doi.org/10.1007/s12517-013-1251-4.

(47) El-Yamani, M. S.; Al-Ramadan, K.; Munnecke, A.; Cantrell, D.; Abdulghani, W.; Reub, L. Microfacies, Depositional Environments and Meter-Scale Cycles of the Middle Jurassic Tuwaiq Mountain

Formation, Central Saudi Arabia. *Journal of African Earth Sciences* **2018**, *145*, 80–101. https://doi.org/10.1016/j.jafrearsci.2018.04.002.

(48) Al-Ramadan, K.; Dogan Ahmet, U.; Muhittin, S. Sedimentology and Diagenesis of the Miocene Nutaysh Member of the Burqan Formation in the Midyan Area (Northwestern Saudi Arabia). *Geological Quarterly* **2013**, *57* (1), 165–174. https://doi.org/10.7306/gq.1081.

(49) Hussain, A.; Morris, E. A.; Al-Ramadan, K.; Shannon, P. M.; Haughton, P. D. W. Hybrid Event Beds (HEBs) and the 'greywacke Problem' Revisited. *Earth-Science Reviews* **2023**, *237*. https://doi.org/10.1016/j.earscirev.2022.104297.

(50) Boles, J. R. Synthesis of Analcime from Natural Heulandite and Clinoptilolite. *American Mineralogist* **1971**, *56* (9–10), 1724–1734.

(51) Kirov, G. N.; Pechigargov, V.; Landzheva, E. Experimental Crystallization of Volcanic Glasses in a Thermal Gradient Field. *Chemical Geology* **1979**, *26* (1–2), 17–28. https://doi.org/10.1016/0009-2541(79)90027-5.

(52) Taylor, M. W. Zeolite Reactions in the Tuffaceous Sediments at Teels Marsh, Nevada. *Clays and Clay Minerals* **1981**, *29* (5), 341–352. https://doi.org/10.1346/CCMN.1981.0290504.

(53) Novembre, D.; Gimeno, D. Synthesis and Characterization of Analcime (ANA) Zeolite Using a Kaolinitic Rock. *Sci Rep* **2021**, *11* (1), 13373. https://doi.org/10.1038/s41598-021-92862-0.

(54) Bello, A. M.; Butt, M. N.; Hussain, A.; Amao, A. O.; Olariu, C.; Koeshidayatullah, A. I.; Malik, M. H.; Al-Hashem, M.; Al-Ramadan, K. Impact of Depositional and Diagenetic Controls on Reservoir Quality

of Syn-Rift Sedimentary Systems: An Example from Oligocene-Miocene Al Wajh Formation, Northwest Saudi Arabia. *Sedimentary Geology* **2023**, 106342. https://doi.org/10.1016/j.sedgeo.2023.106342.

(55) Hughes, G. W.; Filatoff, J. New Biostratigraphic Constraints on Saudi Arabian Red Sea Pre-and Syn-Rift Sequences. In *Middle East Petroleum Geosciences, GEO'94*; Gulf Petrolink: Bahrain, 1995; pp 517-528.

(56) Hughes, G. W. ap G.; Johnson, R. S. Lithostratigraphy of the Red Sea Region. *GeoArabia* **2005**, *10* (3), 49–126. https://doi.org/10.2113/geoarabia100349.

(57) Hussain, A.; Butt, M. N.; Olariu, C.; Malik, M. H.; Koeshidayatullah, A.; Amao, A.; Al-Ramadan, K. Unravelling Reservoir Quality Heterogeneity in Mixed Siliciclastic-Carbonate Deposits: An Example from Miocene Red Sea Rift, NW Saudi Arabia. *Marine and Petroleum Geology* **2022**, *145*, 105850. https://doi.org/10.1016/j.marpetgeo.2022.105850.

(58) Tubbs, R. E.; Fouda, H. G. A.; Afifi, A. M.; Raterman, N. S.; Hughes, G. W.; Fadolalkarem, Y. K. Midyan Peninsula, Northern Red Sea, Saudi Arabia: Seismic Imaging and Regional Interpretation. *GeoArabia* **2014**, *19* (3), 165–184. https://doi.org/10.2113/geoarabia1903165.

(59) Bello, A. M.; Usman, M. B.; Amao, A. O.; Salisu, A. M.; Al-Ramadan, K.; Abubakar, U.; Mukkafa, S.; Kwami, I. A.; Chiroma, L. U.; Al-Hashem, M.; Yusuf, A.; Maigari, A. S.; Kachalla, A.; Aro, O. E.; Ismai'l, M. A.; Umar, U. S.; Akinsanpe, O. T. Linking Provenance and Diagenesis to

Reservoir Quality Evolution of Sandstones: The Paleocene-Eocene Kerri-Kerri Formation, Northeastern Nigeria. *Marine and Petroleum Geology* **2025**, *172*, 1–26. https://doi.org/10.1016/j.marpetgeo.2024.107227.

(60) Bello, A. M.; Salisu, A. M.; Amao, A. O.; Umar, M.; Al-Ramadan, K. Experimental Development of Chlorite: Insights from a Kaolinite Precursor. *Journal of Sedimentary Research* **2025**, *95* (3), 462–484. https://doi.org/10.2110/jsr.2024.099.

(61) Salisu, A. M.; Bello, A. M.; Amao, A. O.; Al-Ramadan, K. The Role of Fluid Chemistry in the Diagenetic Transformation of Detrital Clay Minerals: Experimental Insights from Modern Estuarine Sediments. *Minerals* **2025**, *15* (3), 317. https://doi.org/10.3390/min15030317.

(62) Salisu, A. M.; Bello, A. M.; Amao, A. O.; Lander, R. H.; Al-Ramadan, K. Experimental Study of Smectite Authigenesis and Its Subsequent Illitization: Insights from Modern Estuary Sediments. *Journal of Sedimentary Research* **2025**, *95* (3), 562–588. https://doi.org/10.2110/jsr.2024.135.

(63) Moore, D. M.; Reynolds, R. C., Jr. X-Ray Diffraction and the Identification and Analysis of Clay Minerals. *Geological Magazine* **1998**, *135* (6), 819–842. https://doi.org/https://doi.org/10.1017/S0016756898501501.

(64) Bello, A. M.; Charlaftis, D.; Jones, S. J.; Gluyas, J.; Acikalin, S.; Cartigny, M.; Al-Ramadan, K. Experimental Diagenesis Using Present-Day Submarine Turbidite Sands. *Front. Earth Sci.* **2022**, *10*, 952690. https://doi.org/10.3389/feart.2022.952690.

(65) Sheppard, R. A.; Gude, A. J. *Zeolites and Associated Authigenic Silicate Minerals in Tuffaceous Rocks of the Big Sandy Formation, Mohave County, Arizona*; Professional Paper; Professional Paper 830; U.S. Geological Survey, 1973; pp 1–40.

(66) Renaut, R. W. Zeolitic Diagenesis of Late Quaternary Fluviolacustrine Sediments and Associated Calcrete Formation in the Lake Bogoria Basin, Kenya Rift Valley. *Sedimentology* **1993**, *40* (2), 271–301. https://doi.org/10.1111/j.1365-3091.1993.tb01764.x.

(67) De' Gennaro, M.; Langella, A.; Cappelletti, P.; Colella, C. Hydrothermal Conversion of Trachytic Glass to Zeolite. 3. Monocationic Model Glasses. *Clays and clay miner.* **1999**, *47* (3), 348–357. https://doi.org/10.1346/CCMN.1999.0470311.

(68) Hay, R. L.; Sheppard, R. A. Occurrence of Zeolites in Sedimentary Rocks: An Overview. *Reviews in Mineralogy and Geochemistry* **2001**, *45* (1), 217–234. https://doi.org/10.2138/rmg.2001.45.6.

(69) Coombs, D. S.; Whetten, T. Composition of Analcime from Sedimentary and Burial Metamorphic Rocks1. *Geol Soc America Bull* **1967**, *78* (2), 269. https://doi.org/10.1130/0016-7606(1967)78%5B269:COAFSA%5D2.0.CO;2.

(70) Surdam, R. C.; Boese, S. W.; Crossey, L. J. The Chemistry of Secondary Porosity. In *Clastic Diagenesis*; American Association of Petroleum Geologists, 1984. https://doi.org/10.1306/M37435C8.

(71) Surdam, R. C.; Crossey, L. J.; Hagen, E. S.; Heasler, H. P. Organic-Inorganic Interactions and Sandstone Diagenesis. *American*

Association of Petroleum Geologists Bulletin **1989**, *73* (1), 1–23. https://doi.org/10.1306/703c9ad7-1707-11d7-8645000102c1865d.

(72) Sætre, C.; Hellevang, H.; Dennehy, C.; Dypvik, H.; Clark, S. A Diagenetic Study of Intrabasaltic Siliciclastics Sandstones from the Rosebank Field. *Marine and Petroleum Geology* **2018**, *98*, 335–355. https://doi.org/10.1016/j.marpetgeo.2018.08.026.

Acknowledgments

The authors would like to acknowledge the generous support provided by the College of Petroleum Engineering and Geosciences (CPG), King Fahd University of Petroleum and Minerals, through the Centre for Integrative Petroleum Research (CIPR) (Grant Number: SF24004). The authors are immensely grateful to Mr Habeeb A. Al-Abbas and Mr Bandar D. Al-Otaibi for their assistance in preparing thin sections and running XRD analysis.

Author contributions

A.M. Bello: Conceptualization, Data Curation, Experiments, Formal Analysis, Sampling, Investigation, Methodology, Software, Visualization, Writing – original draft, Writing – review & editing. A.M. Salisu: Data Curation, Experiments, Validation, Visualization, Writing – review & editing. A.O. Amao: Resources, Supervision, Validation, Visualization, Writing – review & editing. O.S. Alade: Experiments, Resources, Validation, Writing– review & editing. M. Mahmoud: Resources, Supervision, Validation, Writing– review & editing. K. Al-Ramadan:

Supervision, Resources, Funding Acquisition, Validation, Visualization, Writing – review & editing.

Data availability

All data supporting the findings of this study are available from the corresponding authors upon reasonable request. Formal data requests may be directed to abdulwahab.bello@kfupm.edu.sa or ramadank@kfupm.edu.sa

Declaration of Competing Interest

The authors declare that they have no known competing financial interests or personal relationships that could have appeared to influence the work reported in this paper.

Funding

This study was funded by the College of Petroleum Engineering & Geosciences (Grant number: SF24004), King Fahd University of Petroleum & Minerals, Dhahran, Saudi Arabia.

Fig. Captions

Fig. 1. (A) Regional view of the Midyan Basin, northwest Saudi Arabia. (B) Location map of the study area showing the Al Wajh outcrop investigated in this study (blue arrow). (C) Stratigraphic column illustrating the age and depositional environment of the Al Wajh Formation. This map was prepared using Adobe Illustrator software, version 22.1 (https://adobe-illustrator-cc.software.informer.com/22.1/).

Fig. 2. Bulk and clay-fraction XRD results for pre- and post-treatment Al Wajh sandstone samples.

(A) Bulk XRD patterns of samples treated with 0.1 M Na_2CO_3, showing detrital quartz, albite, orthoclase, and the development of authigenic analcime. (B) Bulk XRD patterns of samples treated with 0.5 M Na_2CO_3, also indicating the presence of quartz, albite, orthoclase, and authigenic analcime. (C) Clay-fraction XRD of samples treated with 0.1 M Na_2CO_3, showing kaolinite, montmorillonite, illite, chlorite, and the formation of analcime. Note the disappearance of the primary kaolinite peak and the emergence of analcime peaks at 150, 200, and 250 °C.

(D) Clay-fraction XRD of samples treated with 0.5 M Na_2CO_3, showing similar mineral assemblages and changes. The kaolinite peak disappears and analcime peaks appear at the same elevated temperatures.

Fig. 3. SEM images showing the various shapes of analcime crystals, formed during the experiments. (A) Spherical analcime crystals occurring mainly as grain-coating cement. (B) Well-developed cubic analcime crystals. (C-D) Trapezohedral analcime crystals. (E) An aggregate of cubic analcime crystals. (F) An aggregate of polygonal analcime crystals.

Fig. 4. Grain-replacive analcime, analcime, aluminosilica gel, and smectite. (A) Trapezohedral analcime crystal replacing the centre of a pervasively dissolved detrital K-feldspar grain. (B) Incomplete replacement of albite grain by analcime. (C) Well-developed, cubic analcime crystals replacing the edges of an etched K-feldspar grain. (D) Replacement of albite by analcime (E) Replacement of albite by analcime and formation of silica gel from albite dissolution. (F) Development of silica gel from feldspar dissolution and formation of mordenite around the gel. (G) Precipitation of

abundant spherical silica gel on a dissolved feldspar gain. (H) Formation of authigenic smectite around pervasively dissolved K-feldspar grain.

Fig. 5. Clay-replacive analcime crystals. (A) Spherical and cubic analcime crystals replacing smectite and illite. (B) Smooth, well-developed aggregate of polygonal analcime crystals engulfing and replacing kaolinite. (C) An aggregate of analcime crystals rimming and replacing smectite. (D) Analcime aggregate replacing and engulfing illite. (E-F) Pervasive replacement of illite by aggregates of trapezohedral analcime crystals.

Fig. 6. SEM images for other minor zeolites synthesized. (A) SEM image showing the replacement of smectite by rod-like, fibrous mordenite. (B) Replacement of detrital K-feldspar by mordenite. (C-D) SEM images showing the formation of chabazite and mordenite via replacement of smectite. (E) Development of analcime and mordenite around silica gel. (F) Formation of mordenite around silica gel.

Tables Captions

Table 1. Experimental conditions for the autoclave reactions.

Table 2. Semi-quantitative major oxide composition of the synthesized zeolites determined by SEM–EDX analysis.

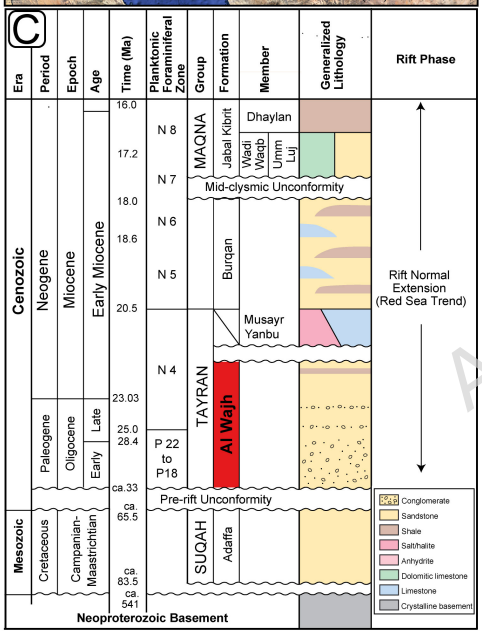

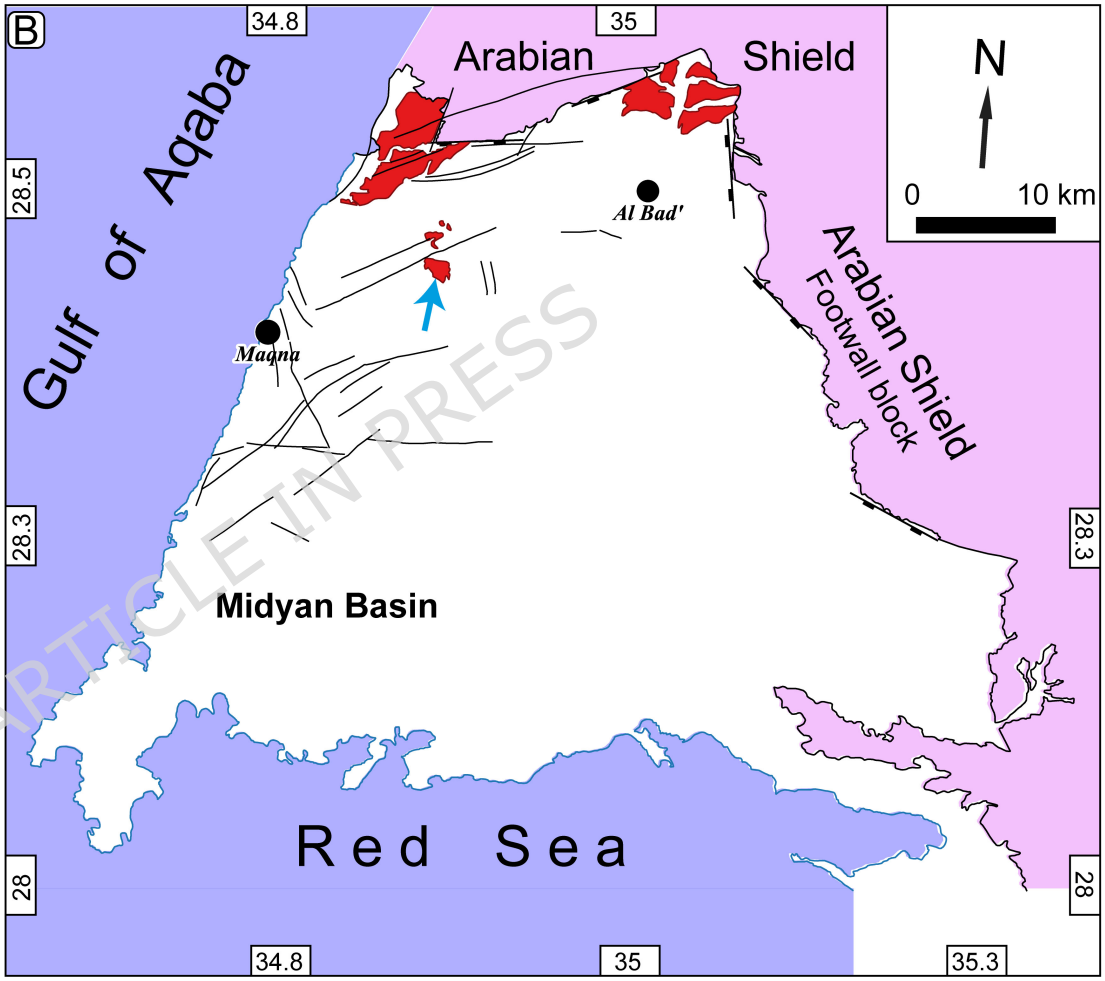

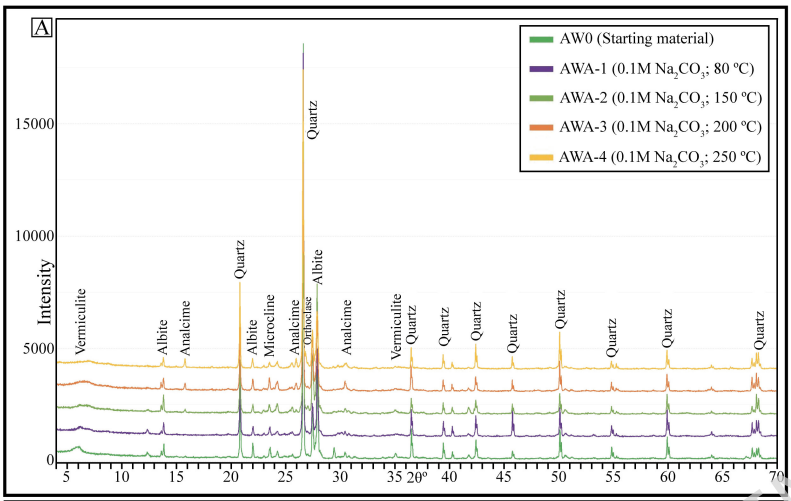

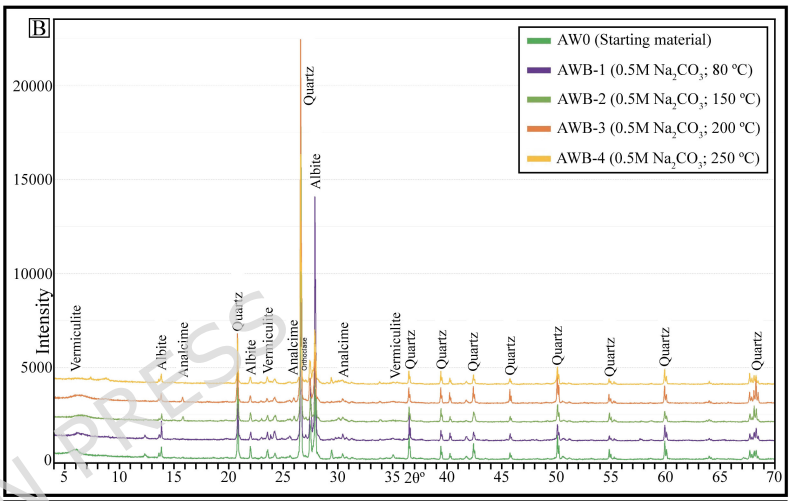

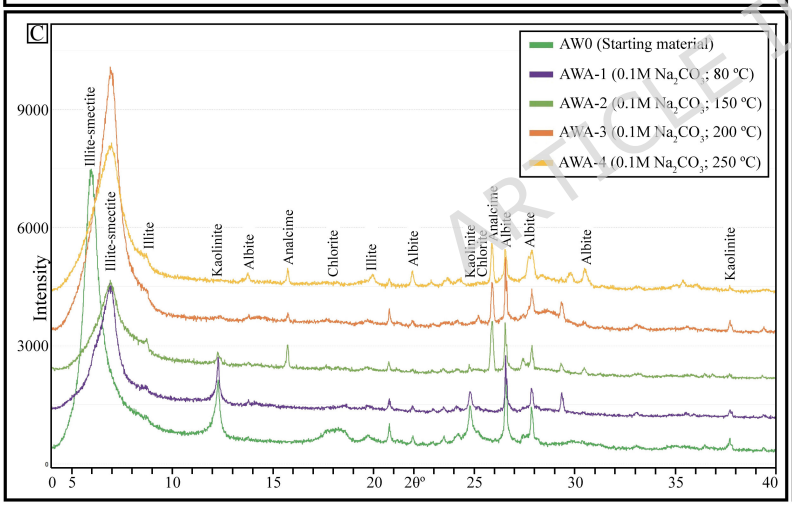

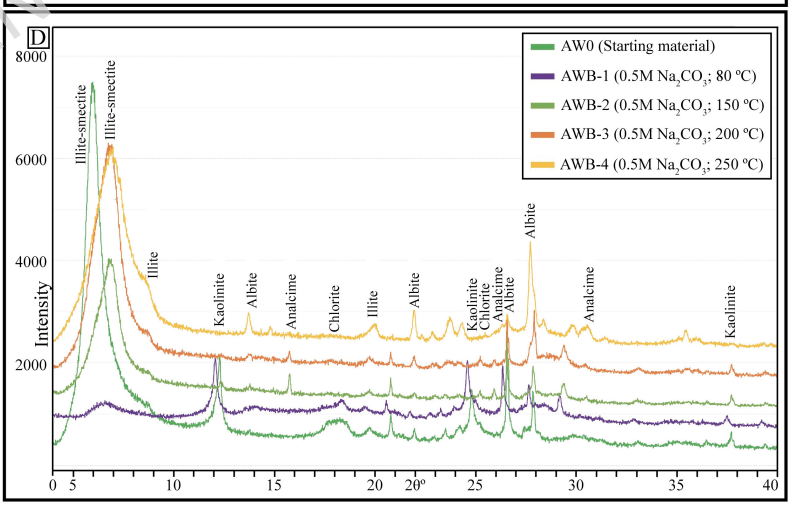

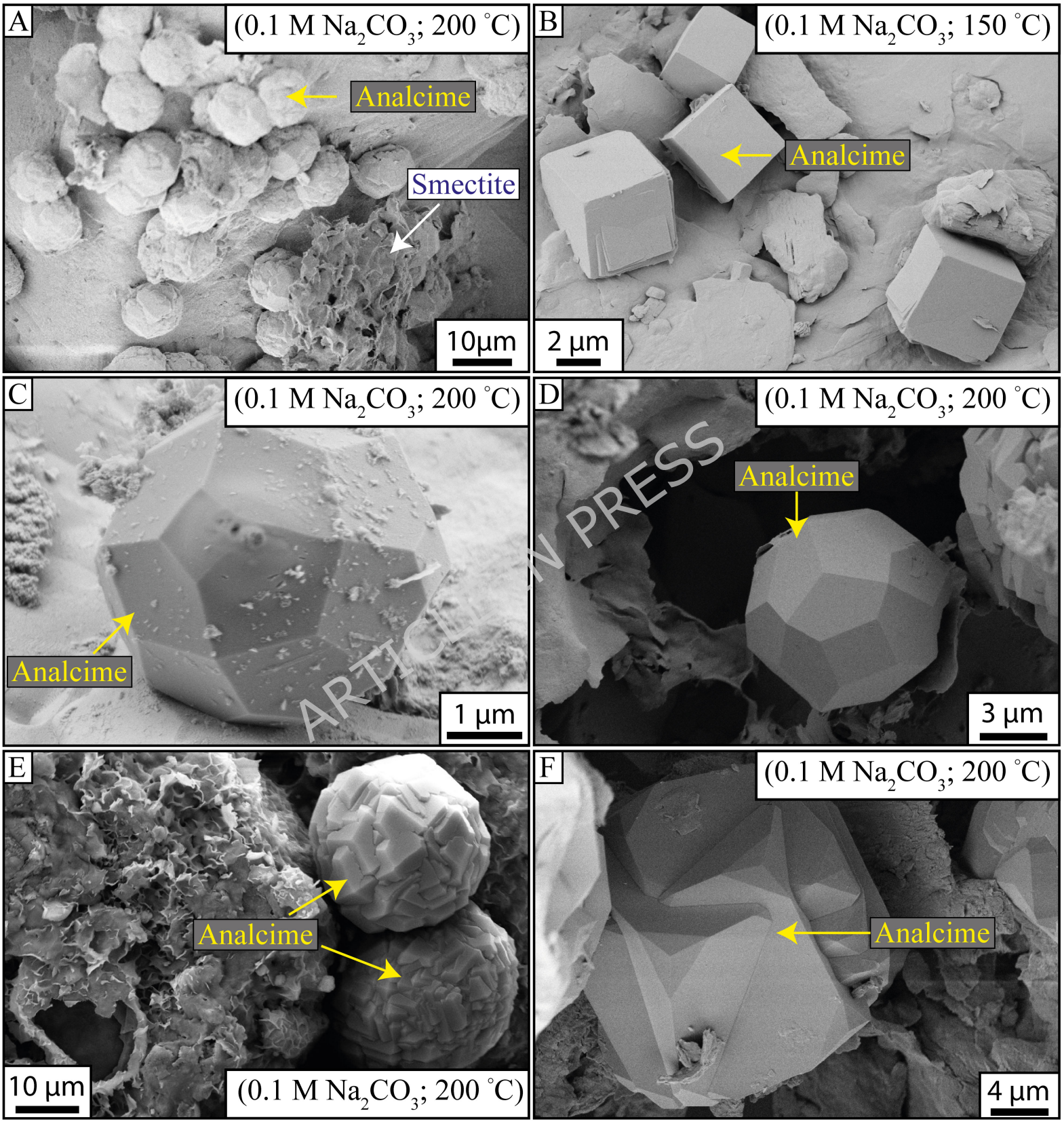

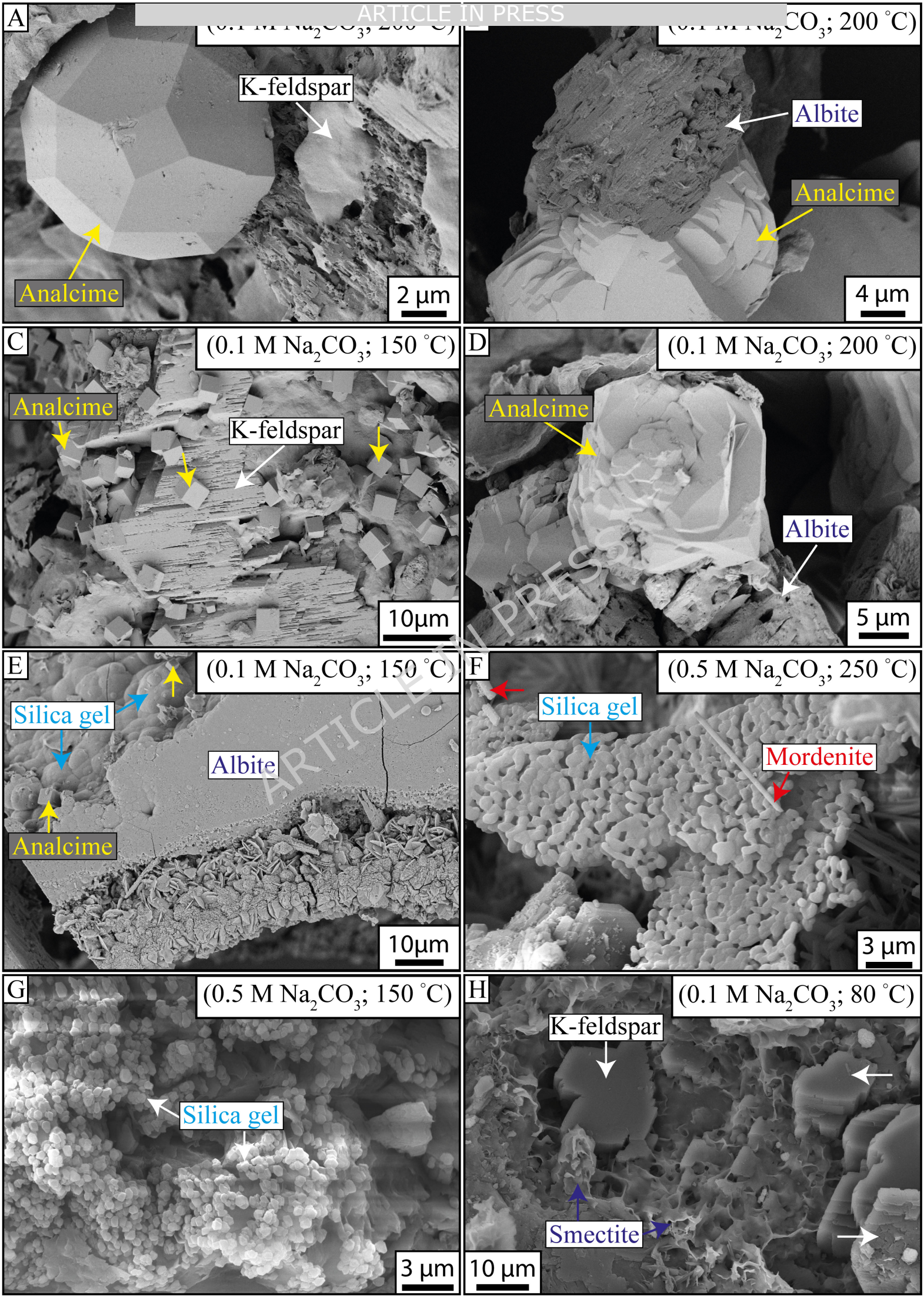

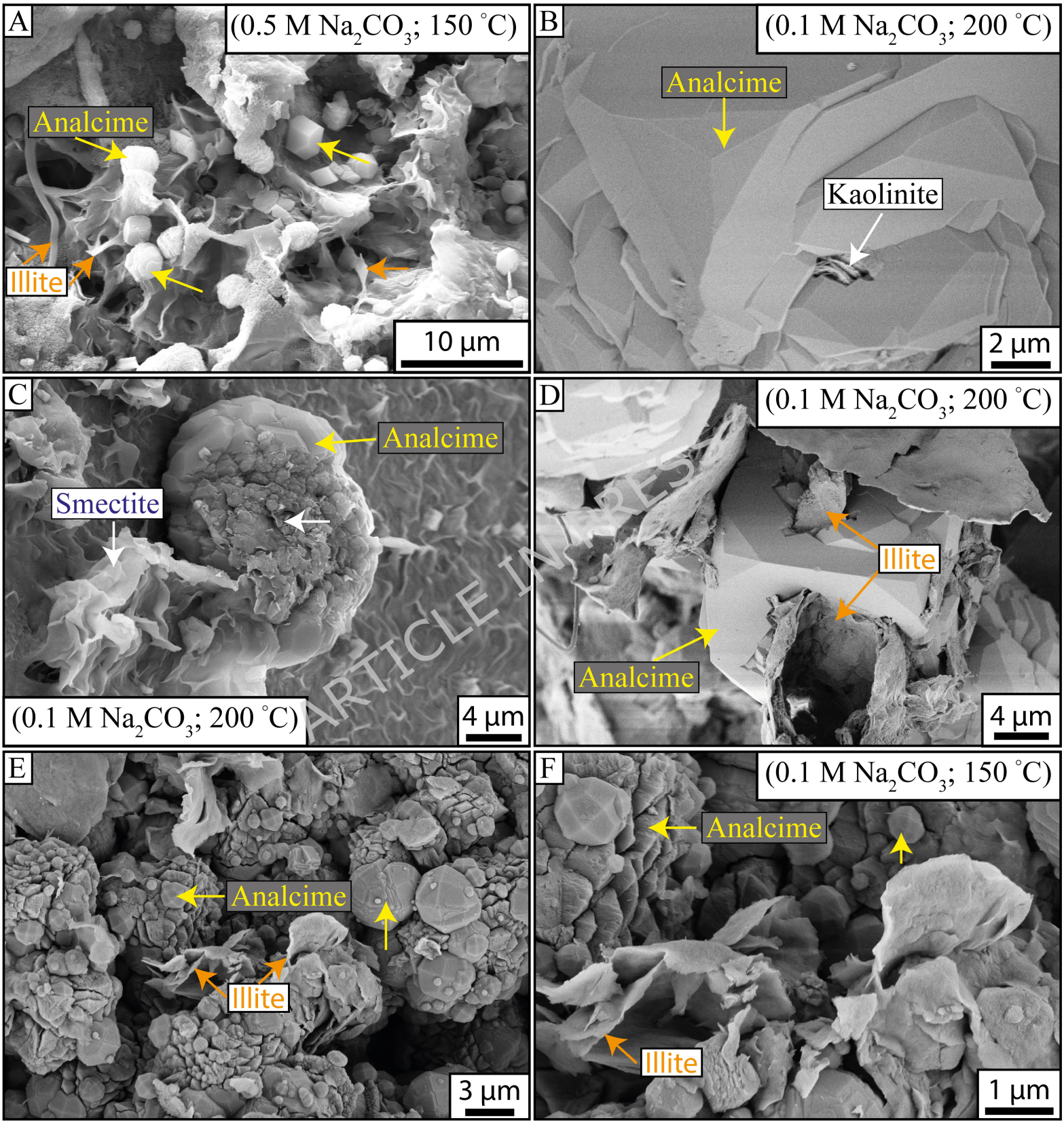

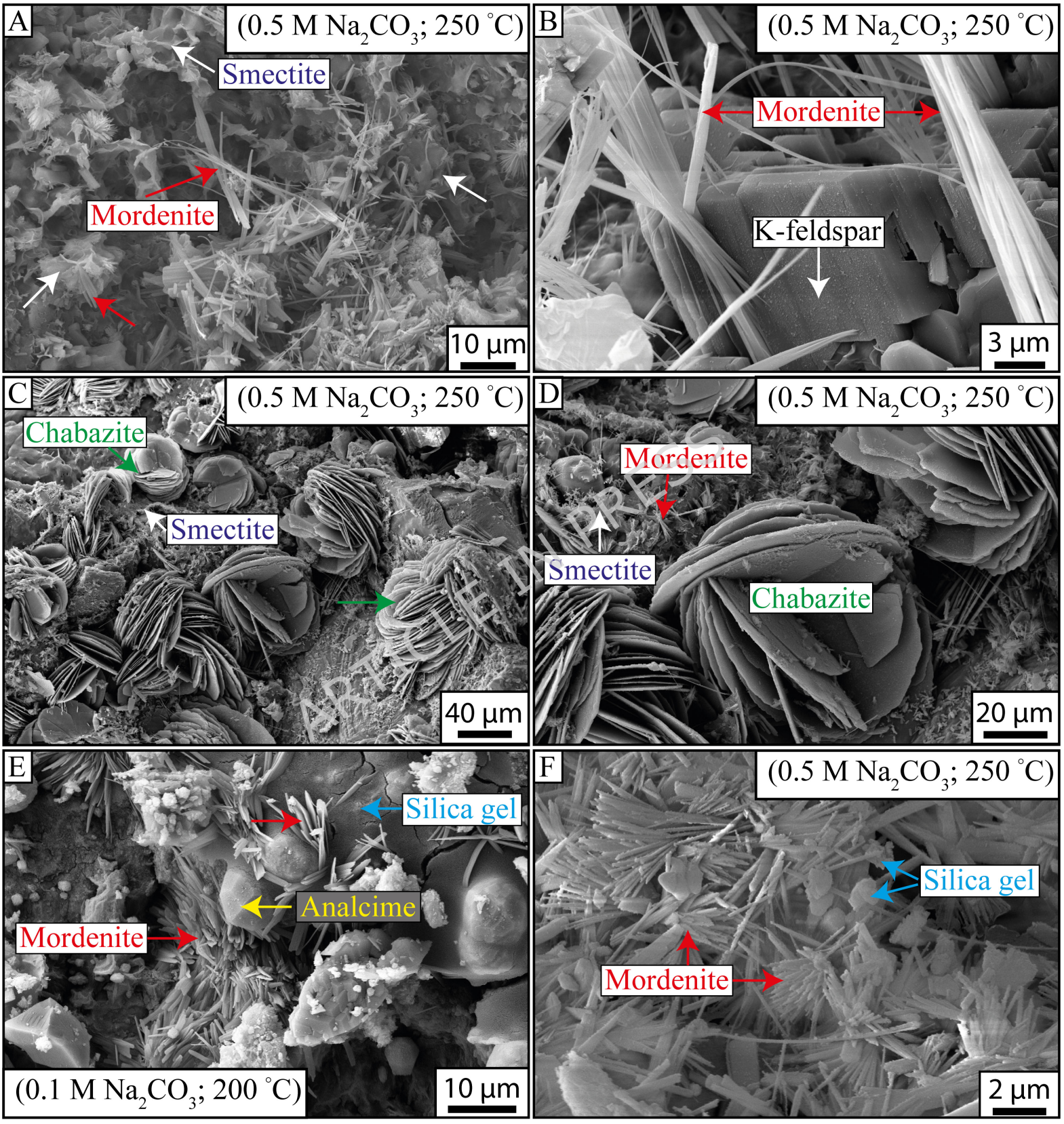

Sample ID	pH (25 °C)	Solution (M)	Temperature (°C)	Final pressure (bar)	Experimental duration (hours)
SF1	11.45	0.1 Na_2CO_3	25		
SF2	11.4	0.5 Na_2CO_3	25		
AWA1	11.15	0.1 Na_2CO_3	80	71.6	336
AWA2	10.33	0.1 Na_2CO_3	150	94.4	336
AWA3	10.12	0.1 Na_2CO_3	200	110.2	336
AWA4	10.07	0.5 Na_2CO_3	250	150.4	336
AWB1	10.92	0.5 Na_2CO_3	80	70.6	336
AWB2	10.6	0.5 Na_2CO_3	150	95.2	336
AWB3	10.45	0.5 Na_2CO_3	200	113.3	336
AWB4	10.09	0.5 Na2CO3	250	148.5	336

Oxide	Analcime [AWA2; n=19]		Analcime [AWA3; n=16]		Analcime [AWA4; n=3]		Analcime [AWB2; n=6]		Analcime [AWB3; n=4]		Analcime [AWB4; n=4]		Mordenite [AWA4; n=6]		Mordenite [AWB3; n=4]		Mordenite [AWB4; n=4]	
	Range	Mean ± SD	Range	Mean ± SD	Range	Mean ± SD	Range	Mean ± SD	Range	Mean ± SD	Range	Mean ± SD	Range	Mean ± SD	Range	Mean ± SD	Range	Mean ± SD
SiO_2	52-70	63 ± 4	63-71	66 ± 2	63-64	64 ± 0	63-68	65 ± 2	63-70	67 ± 3	65-68	67 ± 1	62-66	64 ± 2	36-70	52 ± 12	53-58	56 ± 2
TiO_2	0-0	0 ± 0	0-0	0 ± 0	0-0	0 ± 0	0-0	0 ± 0	0-0	0 ± 0	0-0	0 ± 0	0-2	1 ± 1	0-1	0 ± 0	0-6	2 ± 2
Al_2O_3	19-27	23 ± 3	18-23	21 ± 1	19-20	19 ± 0	18-21	20 ± 1	15-19	17 ± 2	15-20	19 ± 2	3-15	9 ± 4	4-15	10 ± 4	5-13	10 ± 3
FeO	0-4	1 ± 1	0-2	1 ± 1	2-2	2 ± 0	1-3	2 ± 0	2-3	3 ± 1	1-5	2 ± 1	3-12	8 ± 3	4-8	6 ± 1	3-15	8 ± 4
MgO	0-2	0 ± 1	0-1	0 ± 0	0-0	0 ± 0	0-1	0 ± 0	0-1	0 ± 0	0-2	0 ± 1	2-12	7 ± 4	2-8	4 ± 2	4-11	7 ± 3
CaO	0-6	1 ± 2	0-0	0 ± 0	0-0	0 ± 0	0-0	0 ± 0	0-3	1 ± 1	0-1	0 ± 0	0-2	1 ± 1	0-1	0 ± 1	0-1	1 ± 0
Na_2O	6-18	12 ± 3	7-14	12 ± 2	14-14	14 ± 0	8-14	12 ± 2	6-15	10 ± 3	8-13	10 ± 2	7-10	8 ± 1	15-44	25 ± 12	11-18	14 ± 3
K_2O	0-1	0 ± 0	0-0	0 ± 0	0-0	0 ± 0	0-0	0 ± 0	0-0	0 ± 0	0-1	0 ± 0	1-6	2 ± 2	1-1	1 ± 0	1-2	1 ± 0